FRONTIERS OF PHYSICS

RESEARCH ARTICLE
Volume 20 / Issue 3 / 035203 / 2025

Holographic Einstein ring of charged phantom AdS black hole

Gang Chen[1], Ke-Jian He[2], Xiao-Xiong Zeng[2], Man-Jia Liang[3], Li-Fang Li[3,†], Pan Li[3], Peng Xu[3,4,5,6]

1 School of Artificial Intelligence, Chongqing Technology and Business University, Chongqing 400067, China
2 Department of Mechanics, Chongqing Jiaotong University, Chongqing 400000, China
3 Center for Gravitational Wave Experiment, National Microgravity Laboratory, Institute of Mechanics, Chinese Academy of Sciences, Beijing 100190, China
4 Lanzhou Center of Theoretical Physics, Lanzhou University, Lanzhou 730000, China
5 Taiji Laboratory for Gravitational Wave Universe (Beijing/Hangzhou), University of Chinese Academy of Sciences, Beijing 100049, China
6 Hangzhou Institute for Advanced Study, University of Chinese Academy of Sciences, Hangzhou 310024, China
Corresponding author. E-mail: †lilifang@imech.ac.cn
Received November 21, 2024; accepted December 12, 2024

ABSTRACT

Within the framework of AdS/CFT correspondence, this paper studies the holographic shadow images of charged Phantom AdS black holes. Using a Gaussian oscillator source on the AdS boundary, the test waves generated by this source propagate through the black hole spacetime are detected by the response function on the other side of the boundary. The results show that the amplitude of the response function differs for different wave sources and gravitational parameters. From an optical system with a convex lens, we successfully constructed the shadow image of the black hole. When the wave source is located at the South Pole and the observation inclination is zero, a series of axially symmetric concentric circular patterns are always displayed on the screen. As the observation inclination increases, the brightest ring transforms into a ring with distorted brightness, Eventually collapsing to a bright spot. Additionally, the research finds that the shadow image depends not only on the black hole's temperature and chemical potential but also on the frequency of the wave source. Based on the geometric optics, the incidence angle of the photon ring is also discussed, and finds that it Matches the angular distance of the Einstein ring obtained by the holographic framework, which validates the effectiveness of studying Einstein rings through AdS/CFT correspondence.

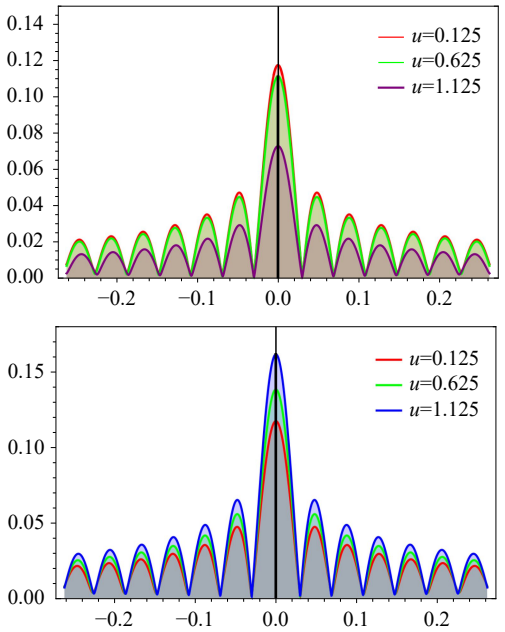

Keywords holographic Einstein ring, phantom AdS black hole, the shadow of black hole

1 Introduction

Since Einstein proposed the theory of general relativity in 1915, it has passed countless observational tests, demonstrating its consistency with observational data. This solidifies its position as the dominant theory for describing gravity today. The theory predicted the existence of black holes and over the years scientists have made great efforts in theoretical analysis and astronomical observation to explore the existence of black holes. To date, high-energy X-ray fluorescence radiation observations from the Cygnus X-1 binary system [1], the gravitational wave signals produced by the merger of binary black holes detected by the Laser Interferometer Gravitational-Wave Observatory (LIGO) [2, 3], and black hole binary systems discovered through radial velocity

https://doi.org/10.15302/frontphys.2025.035203

measurements [4], have strongly confirmed the existence of black holes and marked the astronomical observation into a new era. Excitingly, the Event Horizon Telescope (EHT) collaboration, using very long baseline interferometry (VLBI) technology, successfully captured an image of the supermassive ($M = 6.5 \pm 0.7 \times 10^9 M_\odot$) black hole at the center of the elliptical galaxy Messier (M)87 [5–10]. Additionally, in 2022, the EHT conducted its first horizon-scale radio observation of Sagittarius A* (Sgr A*) at the center of the Milky Way [11–16], and the results showed that the measured error of the Sgr A* ring size is within 10% of the critical curve of the shadow predicted by general relativity.

By analyzing these black hole images, scientists can better understand the accretion processes, jet phenomena, and gravitational field structures of black holes. The ring-like structure formed by radiation from matter captured by the black hole's gravity is known as the "photon ring", while the dark center is the black hole's "shadow" [17, 18]. The black hole shadow not only verifies the correctness of general relativity in strong gravitational fields but also provides important data for studying the physical properties, activity mechanisms, and the surrounding environment of black holes.

Motivated by the importance of black hole shadows, Hashimoto utilized the AdS/CFT correspondence to successfully capture images of black hole shadows in Schwarzschild-AdS spacetime [19, 20]. The work of Hashimoto *et al.* indicates that there is a distinct circular structure in the obtained shadow images, known as the Einstein ring, which corresponds to the position of the photon ring. This work not only provides a new method for studying black hole images but also offers a way for verifying the AdS/CFT correspondence. Then this work extended to charged black holes [21], holographic superconducting models [22], and various gravitational backgrounds [23–31].

In recent years, astronomical observations have indicated that our universe is in a state of accelerated expansion. To explain this phenomenon, physicists have proposed a variety of models. One possible candidate is to modify the theory of gravity without introducing other matter, such as $f(R)$ gravity. Another approach is to introduce an effective field that can produce repulsive gravity. The Phantom field [32–37] is among the latter solution. Studying the properties of black holes within the Phantom field framework can also reveal some novel and interesting phenomena, such as gravitational lensing effects [38, 39], thermodynamics and phase transition behavior [40, 41], holographic thermalization [42], and the motion of spinning particles around black holes [43]. Inspired by these studies, it would be an interesting task to explore whether the holographic shadow images of phantom AdS black holes can be constructed using wave optics methods. In principle, different geometric structures of spacetime naturally lead to different characteristics in the corresponding shadow images. Therefore, to gain a deeper understanding of this relationship, we aim to analyze the effects of changes in temperature, chemical potential, and spacetime structure-related parameters on the features of holographic shadow images.

Our paper is organized as follows. In Section 2, we introduce the construction of the holographic shadow. In Section 3, we briefly review the charged phantom AdS black hole solution and derive its response function. In Section 4, we obtain the holographic Einstein ring and compare the derived results with those obtained in geometric optics in Section 5, which demonstrates that the position of the photon ring obtained from geometric optics is in full agreement with that of the holographic ring.

2 The construction of holographic shadow images

Due to the existence of gravitational lensing, light from distant galaxies becomes distorted when it passes through an intervening galaxy, resulting in arc-shaped or multiple separated images in the observer's field of view. Such a spectacular astronomical phenomenon is known as the Einstein ring. The Einstein ring is not only a direct verification of general relativity on a cosmic scale but also an important tool for studying the mass distribution of giant galaxies, the characteristics of gravitational fields, and the existence of dark matter. Hashimoto *et al.* [19, 20] applied the AdS/CFT correspondence to construct holographic shadow of black holes in Schwarzschild-AdS$_4$ spacetime. Although this study does not directly observe the Einstein ring, it indirectly provides a theoretical framework for understanding complex gravitational phenomena in the universe.

Here we will provide a detailed holographic construction of shadow in the Phantom AdS black hole spacetime. It is important to note that in the global AdS$_4$ spacetime, there is a duality between the $(2+1)$-dimensional conformal field theory (CFT) on the boundary and a black hole, or a massless scalar field in that spacetime. Driven by the time-periodic boundary conditions, the scalar waves generated by this source can propagate from the AdS boundary into the black hole spacetime, as shown in Fig. 1.

We choose an axial symmetric monochromatic oscillating Gaussian source with its position fixed at the South Pole of the AdS boundary $\theta = \pi$. The specific form is as follows:

$$G_{\mathcal{O}}(\mathcal{X}, \theta) = \mathrm{e}^{-\mathrm{i}\varpi\mathcal{X}}\mathcal{M}(\theta), \tag{1}$$

where $\mathcal{M}(\theta) = \frac{1}{2\pi\sigma^2}\exp\left[-\frac{(\pi-\theta)^2}{2\sigma^2}\right]$. Here, $\mathcal{X}$ and θ represent coordinates, and σ is the width of the scalar wave.

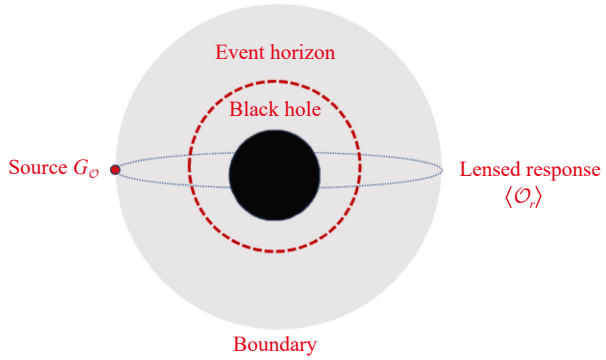

Fig. 1 The schematic of imaging a dual black hole, where the black ball represents the black hole, and the outer edge is the location of the AdS boundary.

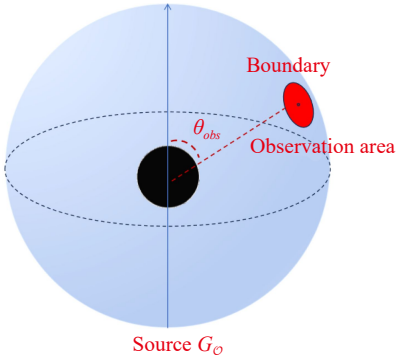

Fig. 2 Construct a schematic of the black hole image through the response function. The black disk in the figure represents the black hole, and the red area on the AdS boundary represents the observation area.

When $\sigma \ll 1$, the above Gaussian function is decomposed into a scalar spherical harmonics which is expressed as follows:

$$\mathcal{M}(\theta) \simeq \sum_{\varsigma=0}^{\infty} C_{\varsigma 0} Y_{\varsigma 0}(\theta). \tag{2}$$

Here the coefficient $C_{\varsigma 0}$ of the spherical harmonics function $Y_{\varsigma 0}$ can be written as

$$C_{\varsigma 0} \equiv (-1)^{\varsigma} \sqrt{\frac{\varsigma + \frac{1}{2}}{2\pi}} \exp\left[-\frac{1}{2}\left(\varsigma + \frac{1}{2}\right)^2 \sigma^2\right], \tag{3}$$

where ς in Eq. (3) represents the magnetic quantum number. When probe waves propagate through the spacetime structure of a black hole, they undergo diffraction due to the strong gravitational effects of the black hole and eventually reach other locations on the AdS boundary, producing the corresponding response function $\langle \mathcal{O}(x) \rangle$ shown in Fig. 2. We transform the obtained response function $\langle \mathcal{O}(x) \rangle$ into an intuitive image, a virtual optical system located in three-dimensional space is needed. This system consists of an extremely thin convex lens and a spherical screen, as shown in Fig. 3. From Fig. 2, we extract the local response function indicated by the red circle with a radius of L and then map it onto this virtual imaging system for processing. In this process, the response function $\langle \mathcal{O}(x) \rangle$ and the image $\Psi_S(\bar{x}_S)$ presented on the spherical screen satisfy the following relationship [19, 20]:

$$\Psi_S(\bar{x}_S) = \int_{|\bar{x}|<d} \mathrm{d}^2 x W_f \langle \mathcal{O}(\bar{x}) \rangle \mathrm{e}^{-\frac{\mathrm{i}\varpi}{f} \bar{x} \cdot \bar{x}_S}. \tag{4}$$

In the above formula, $\bar{x} = (x, y, z)$ and $\bar{x}_S = (X_S, Y_S, Z_S)$ represent the Cartesian-like coordinates on the boundary and on the spherical screen, respectively. W_f refers to the window function which is as follows:

$$W_f \equiv \begin{cases} 1, & 0 \leq |\ \bar{x}\ | \leq d, \\ 0, & |\ \bar{x}\ | > d. \end{cases} \tag{5}$$

In this process, the convex lens can be regarded as a converter that transforms plane waves into spherical waves and projects them onto the curved screen, as illustrated in Fig. 3. The imaging system is located within the observation area and the size d of the lens is much smaller than the focal length f. Adjust the imaging system to meet the conditions:

$$(x_S, y_S, z_S) \equiv (x, y, z) | x^2 + y^2 + z^2 = f^2. \tag{6}$$

Next, we will construct the shadow image of the Phantom AdS black hole within the framework of general relativity, based on Eq. (4).

3 Charged phantom AdS black hole response function

As previously mentioned, extracting the response function

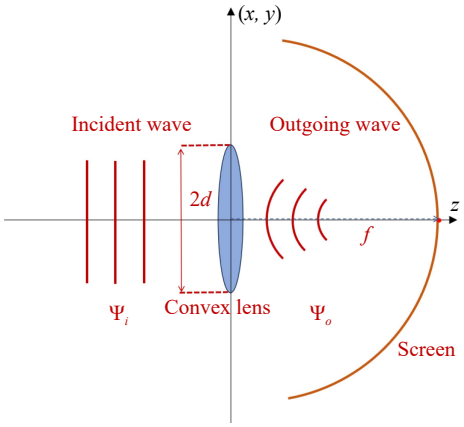

Fig. 3 The role of virtual optical systems in constructing holographic images.

is a key step in constructing the holographic shadow images. In this section, we will obtain the required response function effectively in the context of Phantom AdS black hole spacetime. The Phantom AdS black hole can be solved through the following action [40]:

$$S=\int \mathrm{d}^4x\sqrt{-g}\left(R+2\eta F_{\mu\nu}F^{\mu\nu}+2\Lambda\right). \tag{7}$$

the cosmological constant $\Lambda=-\frac{3}{L^2}$, where L is the radius of the AdS spacetime. The parameter η characterizes the properties of the electromagnetic field. Specifically, when $\eta=1$, it corresponds to the Maxwell field, and when $\eta=-1$, it corresponds to a spin-1 Phantom field. Solving the equations of motion derived from Eq. (7) yields a solution

$$\mathrm{d}s^2=-f(r)\mathrm{d}t^2+\frac{\mathrm{d}r^2}{f(r)}+r^2(\mathrm{d}\theta^2+\sin^2\theta\mathrm{d}\psi^2), \tag{8}$$

and

$$F=-\frac{q}{r^2}\mathrm{d}r\wedge\mathrm{d}t, \tag{9}$$

$$f(r)=1-\frac{2\mathcal{M}}{r}+\frac{\eta q^2}{r^2}+\frac{r^2}{L^2}. \tag{10}$$

Here $\mathcal{M}$ represents the mass of the black hole, and q represents the charge of the source. When all parameters are zero, the solution will degenerate into Minkowski spacetime. When $\Lambda<0$, the solution is asymptotically anti-de Sitter spacetime, and when $\eta=1$, it reverts to the Reissner–Nordström-AdS (RN-AdS) black hole. Solving the equation $f(r)=0$ yields two positive real roots for $\eta=1$ (corresponding to the event horizon and inner horizon), while $\eta=-1$ has only one positive real root (corresponding to the event horizon) [40]. In this spacetime background, we can obtain the specific forms of the mass $\mathcal{M}$, Hawking temperature T_h, and electric potential A_t as follows:

$$\mathcal{M}=\frac{1}{2}r_h\left(1+\frac{\eta q^2}{r_h^2}+\frac{r_h^2}{L^2}\right). \tag{11}$$

$$T_h=\frac{r_h^4-\eta q^2+r_h^2L^2}{4\pi L^2r_h^3}. \tag{12}$$

$$A_t=\frac{q}{r_h}. \tag{13}$$

Introduce an affine parameter $\chi=1/r$, which makes $f(r)=\frac{1}{\chi^2}f(\chi)$, Eq. (8) can be re-expressed as

$$\mathrm{d}s^2=\frac{1}{\chi^2}[-f(\chi)\mathrm{d}t^2+f^{-1}(\chi)\mathrm{d}\chi^2+\mathrm{d}\theta^2+\sin\theta^2\mathrm{d}\psi^2]. \tag{14}$$

The parameter $\chi_h=1/r_h$ represents the event horizon of the black hole. We consider a complex scalar field Φ_c as the probe field. The dynamics of the particles in the scalar field satisfy the Klein–Gordon equation:

$$D_aD^a\Phi_c-m^2\Phi_c=0, \tag{15}$$

where

$$D_a=\nabla_a-\mathrm{i}\bar{e}A_a. \tag{16}$$

$\bar{e}$ represents the charge of the complex scalar field. For simplicity, the infalling Eddington coordinates are used to solve the above Klein–Gordon equation:

$$v\equiv t+\chi_*=t-\int\frac{1}{f(\chi)}\mathrm{d}\chi. \tag{17}$$

Thus the metric function (14) can be rewritten as

$$\mathrm{d}s^2=\frac{1}{\chi^2}\left(-f(\chi)\mathrm{d}v^2-2\mathrm{d}v\mathrm{d}\chi+\mathrm{d}\theta^2+\sin^2\theta\mathrm{d}\psi^2\right). \tag{18}$$

Near the AdS boundary, the scalar field Φ_c behaves as

$$\Phi_c(v,\chi,\theta,\psi)=J_{\mathcal{O}}(v,\theta,\psi)+\chi\partial_vJ_{\mathcal{O}}(v,\theta,\psi)+\frac{1}{2}\chi^2D^2{}_SJ_{\mathcal{O}}(v,\theta,\psi)+\chi^3\langle\mathcal{O}\rangle. \tag{19}$$

In Eq. (19), $D^2{}_S$ represents the scalar Laplacian on the unit S^2 sphere. According to the AdS/CFT dictionary, $J_{\mathcal{O}}$ and $\langle\mathcal{O}\rangle$ in Eq. (19) are independent functions of the boundary coordinates. Taking $J_{\mathcal{O}}$ as the source, the expectation value of the corresponding dual operator is the response function $\langle\mathcal{O}\rangle_{J_{\mathcal{O}}}$ which is written as

$$\langle\mathcal{O}\rangle_{J_{\mathcal{O}}}=\langle\mathcal{O}\rangle-(\partial_v-\mathrm{i}u)J_{\mathcal{O}}. \tag{20}$$

The parameter u represents the chemical potential with the specific form $u=q/r_h$. Considering the symmetry of the spacetime background, we expand Φ_c as

$$\Phi_c(v,\chi,\theta,\psi)=\mathrm{e}^{-\mathrm{i}\omega v}\sum_{\varsigma=0}^{\infty}c_{\varsigma0}Z_\varsigma(\chi)Y_{\varsigma0}(\theta), \tag{21}$$

where Z_ς satisfies

$$0=\chi^2f(\chi)Z_\varsigma''+\chi^2\left[f'(\chi)+2\mathrm{i}(\omega-\bar{e}A)\right]Z_\varsigma'+\left[(2-2f(\chi))+\chi f'(\chi)-\chi^2\varsigma(\varsigma+1)-\mathrm{i}\bar{e}\chi^2A'\right]Z_\varsigma. \tag{22}$$

Here $f'(\chi)=\frac{\partial}{\partial\chi}f(\chi)$ and the asymptotic behavior of Z_ς at the AdS boundary is defined as

$$Z_\varsigma=1+\chi\langle\mathcal{O}\rangle_\varsigma+\mathcal{O}(\chi^2). \tag{23}$$

Therefore the corresponding response function is

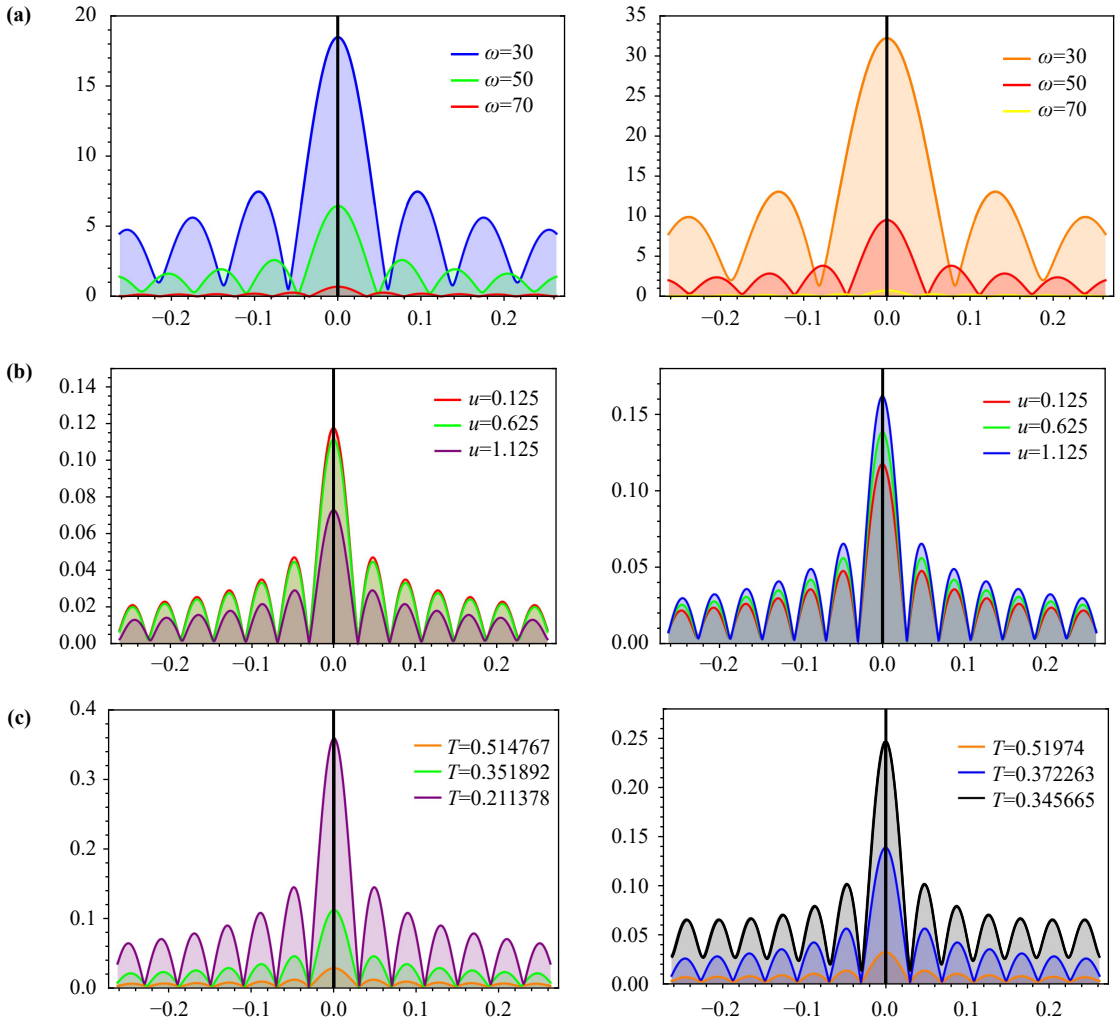

Fig. 4 **(a)** The absolute amplitude change of the total response function when the source frequency ω is different and the chemical potential u is fixed at $u = 0.625$. **(b)** The absolute amplitude change of the total response function when the chemical potential u takes a different value and the source frequency ω is fixed at $\omega = 80$. **(c)** The absolute amplitude change of the total response function when the boundary temperature T takes different values and the source frequency ω is fixed as $\omega = 80$. Here, the left panel shows the parameter $\eta = 1$, while the right panel illustrates $\eta = -1$.

$$\langle \mathcal{O} \rangle_{J_{\mathcal{O}}} = \mathrm{e}^{-\mathrm{i}\omega v} \sum_{\varsigma=0}^{\infty} C_{\varsigma 0} \langle \mathcal{O} \rangle_{J_{\mathcal{O}\varsigma}} Y_{\varsigma 0}(\theta), \tag{24}$$

and

$$\langle \mathcal{O} \rangle_{J_{\mathcal{O}\varsigma}} = \langle \mathcal{O} \rangle_{\varsigma} + \mathrm{i}\bar{\omega}, \tag{25}$$

where $\bar{\omega} = \omega + u$. Then Eq. (22) is solved with the help of two key boundary conditions. The first is at the AdS boundary $Z_{\varsigma}(0) = 1$. The second condition is the regular boundary condition at the event horizon

$$\left[\chi_h^2 f'(\chi_h) + 2\mathrm{i}\omega\chi_h^2\right] Z_{\varsigma}' - \left[2\mathrm{i}\omega\chi_h + \varsigma(\varsigma+1)\chi_h^2\right] Z_{\varsigma} = 0. \tag{26}$$

Based on the above analysis, the pseudo-spectral method can be employed to obtain the numerical results for Z_{ς}, and subsequently extract the required $\langle \mathcal{O} \rangle_{\varsigma}$ [21]. And then we can further obtain the response function $\langle \mathcal{O} \rangle_{J_{\mathcal{O}\varsigma}}$. Next, we examined the changes in the response function when the Gaussian source frequency ω, chemical potential u, and parameter η take different values. When the parameters $\eta = 1$ and $\eta = -1$, Fig. 4 shows the response functions with different values for the related parameters. In Fig. 4(a), the source frequencies are taken as $\omega = 30, 50, 70$, regardless of whether the parameter η takes the value of 1 or –1. It is worth noting that the amplitude peaks of the response function for $\eta = -1$ are larger than those of $\eta = 1$, and their oscillation periods are higher than the latter. In Fig. 4(b), we show the chemical potential u continues to increase, the amplitude of the response function decreases for $\eta = 1$ while the amplitude of the response function increases for $\eta = -1$.

Additionally, we discuss the effect of the temperature

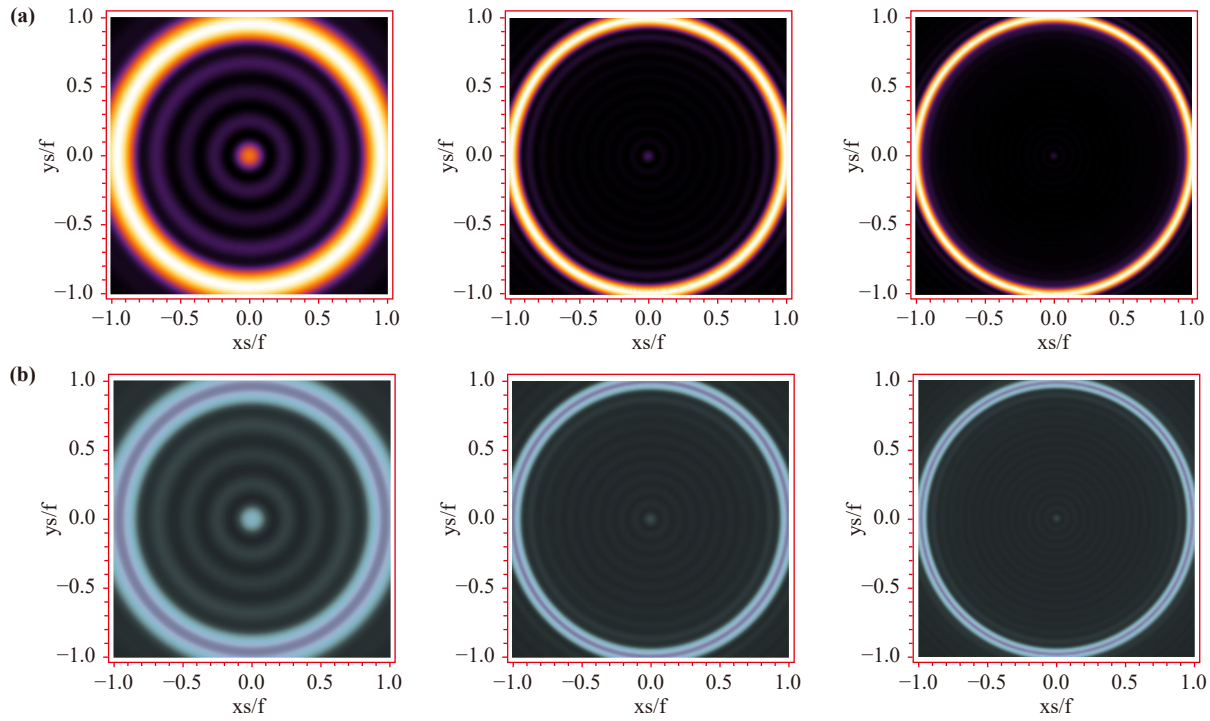

Fig. 5 **(a)** The density maps of the lensed response on the screen for different ω at the observational angle $\theta_O = 0$ with $\eta = 1$, $q = 0.5$, and $r_h = 0.8$. **(b)** The density maps of the lensed response on the screen for different ω at the observational angle $\theta_O = 0$ with $\eta = -1$, $q = 0.5$ and $r_h = 0.8$. The values of frequency ω from the left panel to the right panel are $\omega = 25,\ 55,\ 80$, respectively.

T on the response function which is shown in Fig. 4(c). For different black hole event horizon radii $r_h = 2,\ 1.25,\ 0.67$, the corresponding boundary temperatures T are $T = 0.514767,\ 0.351892,\ 0.211378$ respectively for $\eta = 1$ and $q = 0.5$. And for $\eta = -1$ and $q = 0.5$, the boundary temperatures T are $T = 0.51974,\ 0.372263,\ 0.345665$ for the same radii. In both cases of $\eta = 1$ and $\eta = -1$, the increase of the temperature T leads to a decrease in the response function amplitude. For $\eta = 1$, the amplitude of the response function changes significantly with temperature T. For example, when $T = 0.211378$, the amplitude reaches its peak and moves downward well at $T = 0.351892$ and 0.514767, which means an increase in temperature T will lead to a decrease in the response function. When $\eta = -1$, the amplitude of the response function still maintains a decreasing trend with the increase of temperature T, which is similar to the case of $\eta = 1$. Although the black hole has the same event horizon r_h, due to the different values of the parameter η, there is a difference in the boundary system temperature, so the decrease in the amplitude peak of the response function is more obvious in the case of $\eta = 1$.

4 Holographic Einstein rings of a phantom AdS black hole

The response function contains a wealth of spacetime information. With the above response function and the virtual optical system shown in Fig. 3, we can transform the obtained response function into an intuitive image form. By appropriately selecting the specific parameters, we numerically simulated the holographic image of the Phantom AdS black hole and plotted the corresponding brightness curves. Here we set $\sigma = 0.05$ and $d = 0.6$.

We present the holographic images of the Phantom AdS black hole when the wave source frequency ω takes values of $\omega = 25,\ 55,\ 80$, as shown in Figs. 5(a, b). A series of bright concentric circular structures are observed, among which this brightest ring is known as the holographic Einstein ring. When $\eta = 1$, as the wave source frequency ω increases, the width of the ring decreases while the radius of the ring increases. When $\eta = -1$, the changes in the wave source frequency ω have a similar effect on the ring as when $\eta = 1$, but in this case, the increase in the ring radius of the ring is more obvious. In Figs. 6(a, b), we plotted the brightness curves similar to Figs. 5(a, b). The horizontal axis represents the position of the brightness curve, while the vertical axis indicates its intensity. We find that the changes in the wave source frequency affect both the magnitude and the position of the peak. Specifically, when $\eta = 1$, as the wave source frequency ω increases, the highest peak value in the brightness curve significantly decreases, and its position gradually moves away from the center of the screen, which implies that the radius of

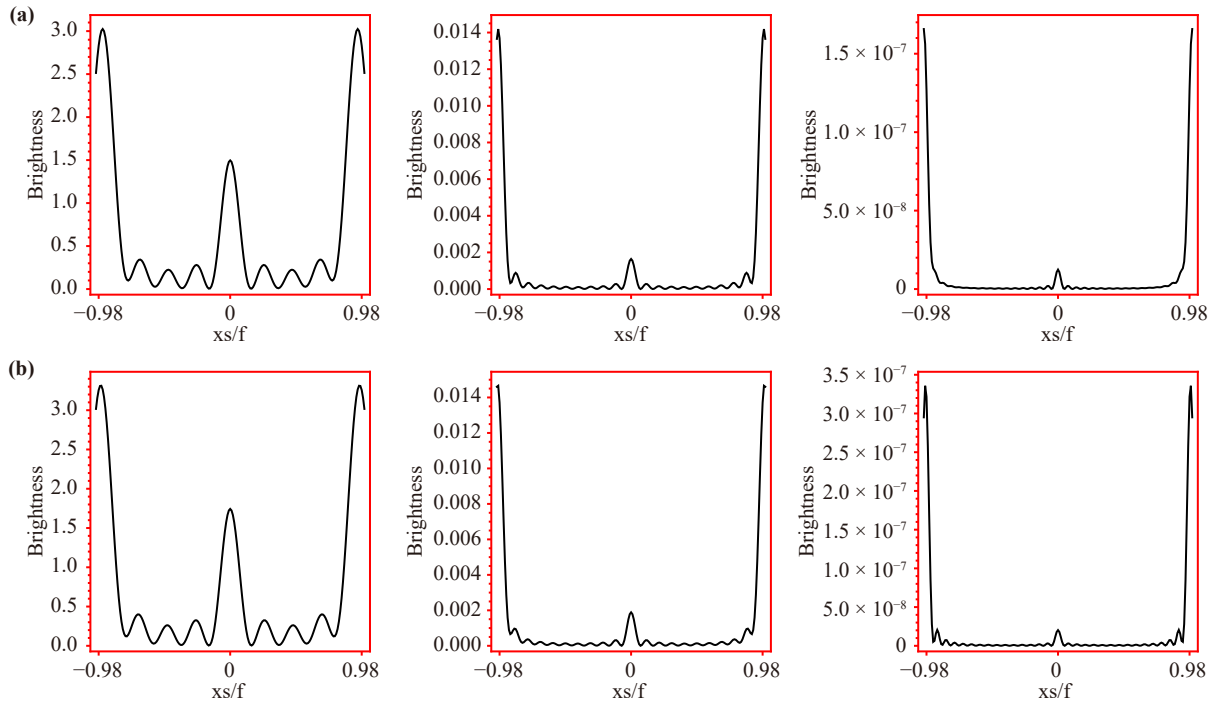

Fig. 6 **(a)** Changes in brightness of the lensed response on the screen for different ω with $\eta = 1$, $q = 0.5$, and $r_h = 0.8$. **(b)** Changes in brightness of the lensed response on the screen for different ω with $\eta = -1$, $q = 0.5$, and $r_h = 0.8$. The values of frequency ω from the left panel to the right panel are $\omega = 25,\ 55,\ 80$, respectively.

the brightest ring is gradually increasing. Conversely, when $\eta = -1$, although the overall trend of the brightness curve with frequency changes is similar to when $\eta = 1$, there are some differences. The highest peak value is slightly higher than the case in $\eta = 1$, and the peak position moves slowly away from the center of the screen. Furthermore, as the frequency is gradually increased, the brightness curve exhibits increasingly sharp characteristics, which matches the phenomenon shown in Figs. 5(a, b). The reason behind this is that within the framework of geometric optics approximation, the high-frequency conditions can be accurately captured.

Figures 7(a, b) present the holographic shadow of the Phantom AdS black hole with the different chemical potential u for $\eta = 1$ and -1. We fix at $r_h = 0.8$ and $\omega = 80$ and the chemical potential $u = 0.125,\ 0.625$, and 1.125. For $\eta = 1$, the image still exhibits a bright ring structure. As the chemical potential u increases, the brightness of the brightest ring gradually decays and its radius also shows decreases, although this decrease is not very obvious. For the case $\eta = -1$, the change in the brightness of the brightest ring is the opposite of the case for $\eta = 1$. It significantly increases with the increase of the chemical potential u. Similarly, the radius of the brightest ring also shows a decreasing trend, which is consistent with the behavior observed when $\eta = 1$.

The corresponding brightness curves are displayed in Figs. 8(a) and (b). The results show that, under the condition of $\eta = 1$, the maximum peak value of the brightness curve decreases with the increase of the chemical potential u, while its position exhibits a trend of gradually moving away from the center of the screen. However, this trend is not easily observable by the naked eye, indicating that although the radius of the bright ring is affected by the chemical potential, the change is quite minimal. In contrast, under the condition of $\eta = -1$, the maximum peak value of the brightness curve significantly increases with the increase of the charge q, and its position still shows a trend of moving away from the center of the screen.

Next, we discuss the impact of boundary temperature T on the holographic images of black holes shown in Figs. 9(a, b). We set $q = 0.5$ and $\omega = 80$. In Fig. 9(a), when $\eta = 1$, the temperature T takes a smaller value $T = 0.119366$, the produced ring is closer to the center of the screen. When the temperature increases to $T = 0.211378$ and $T = 0.514767$, the corresponding bright ring moves towards the screen's edge, but not very obvious. In Fig. 9(b) with $\eta = -1$, as the temperature T increases, the produced ring also moves towards the screen's edge and this behavior is more obvious than the case $\eta = 1$. That is to say, for both $\eta = 1$ and $\eta = -1$, the radius of the brightest ring increases with the increase of temperature T, but the increase is different. This effect can also be observed in Figs. 10(a, b), where the peak brightness curves gradually move towards the boundary with the increase of temperature T. Additionally, when the temperature T is low ($T = 0.119366$), there is also a

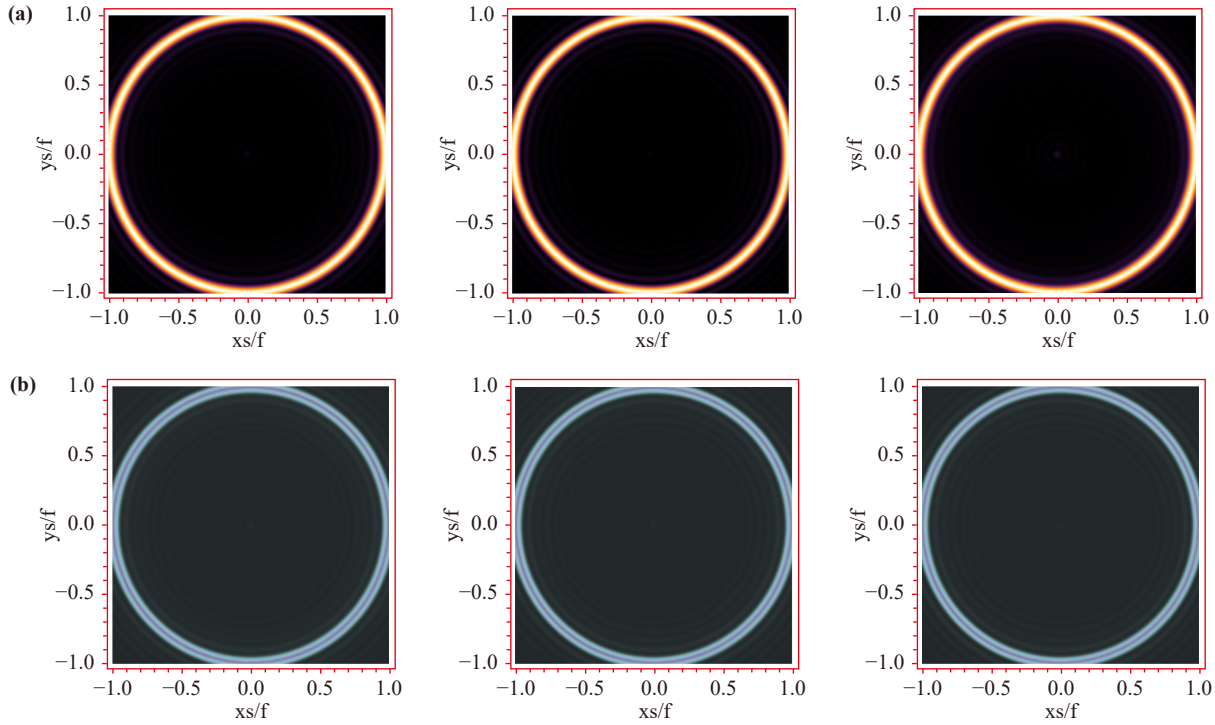

Fig. 7 **(a)** The density maps of the lensed response on the screen for different chemical potential u at the observational angle $\theta_O = 0$ with $\eta = 1$, $\omega = 80$ and $r_h = 0.8$. **(b)** The density maps of the lensed response on the screen for different chemical potential u at the observational angle $\theta_O = 0$ with $\eta = -1$, $\omega = 80$ and $r_h = 0.8$. The values of chemical potential u from the left panel to the right panel are $u = 0.125,\ 0.625,\ 1.125$.

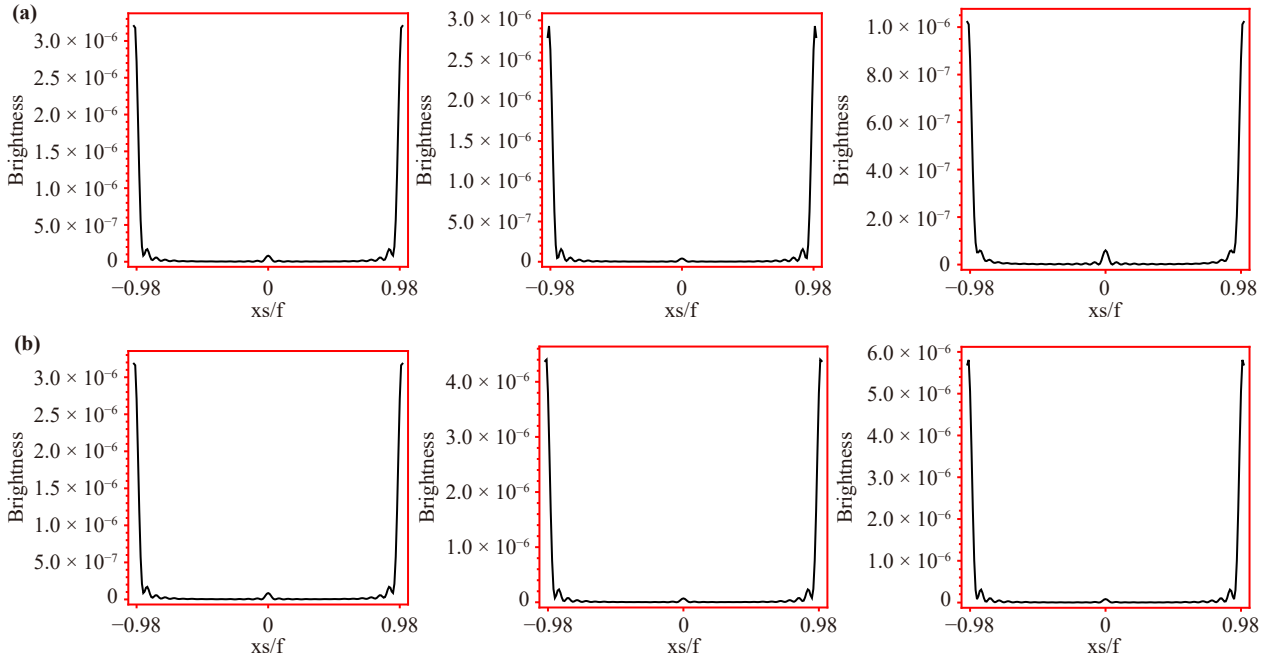

Fig. 8 **(a)** Changes in brightness of the lensed response on the screen for different ω with $\eta = 1$, $\omega = 80$ and $r_h = 0.8$. **(b)** Changes in brightness of the lensed response on the screen for different ω with $\eta = -1$, $\omega = 80$ and $r_h = 0.8$. The values of chemical potential u from the left panel to the right panel are $u = 0.125,\ 0.625,\ 1.125$, respectively.

peak in the brightness curve at the center of the screen, which corresponds to a bright spot on the screen shown in Fig. 9(a).

All the previous discussions focus on the wave source

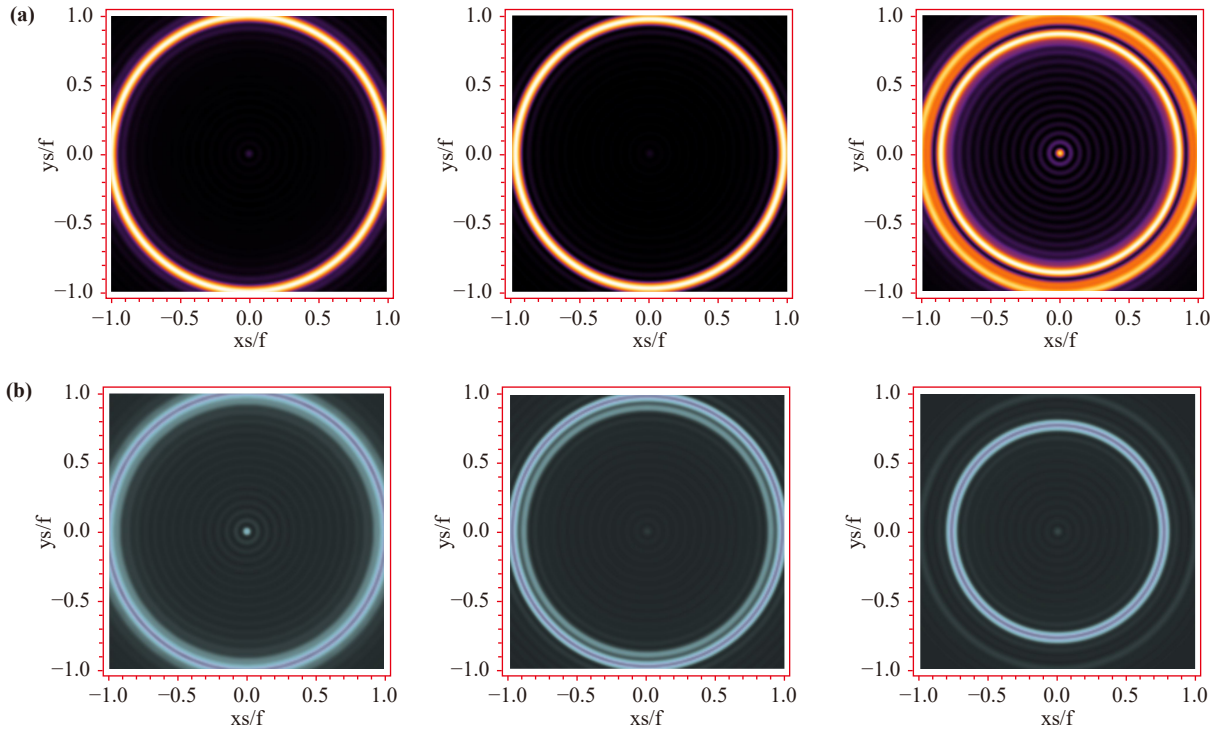

Fig. 9 **(a)** The density maps of the lensed response on the screen for different temperatures T at the observational angle $\theta_O = 0$ with $\eta = 1$, $\omega = 80$, and $q = 0.5$. The values of temperature T from the left panel to the right panel are $T = 0.514767,\ 0.211378,\ 0.119366$. **(b)** The density maps of the lensed response on the screen for different temperatures T at the observational angle $\theta_O = 0$ with $\eta = -1$, $\omega = 80$, and $q = 0.5$. The values of temperature T from the left panel to the right panel are $T = 0.514767,\ 0.351892,\ 0.211378$, respectively.

at the fixed position. By carefully comparing the image features at different observation positions, we can more accurately identify the specific impact of the relevant parameters on the spacetime geometry.

First, we consider $\eta = 1$ with different charges. and the system charge q varies. In Fig. 11, the results indicate that when the observation angle $\theta_O = \pi/6$, the original axial symmetric structure is broken, replaced by light arcs located on the left and right sides of the image. The brightness of the right light arc is higher than that of the left light arc. Additionally, as the charge increases, the brightness of the left light arc gradually increases, especially when $q = 0.5$. The brightness of the left light arc is brighter than that of $q = 0.1$. When the observation angle changes to $\theta_O = \pi/3$, the left light arc area of the image almost disappears, and the right light arc changes into a smaller arc structure. When the observation angle increases to $\theta_O = \pi/2$, only an isolated bright spot appears on the right side of the image.

A similar lens response image for $\eta = -1$ is shown in Fig. 12. It is not difficult to observe that the axial symmetric circular structure gradually transforms into light arcs, and eventually evolves into an isolated bright spot on the right side of the screen as the observer changes its position, which is similar to the case for $\eta = 1$.

5 Comparison between photon rings and einstein rings

In this section, we will use geometrical optics to analyze the brightest ring in the shadow image. The motion of photons near a charged AdS black hole can be precisely described by the Lagrangian shown as follows:

$$\mathcal{L} = \frac{1}{2} g_{\mu\nu} \left(\dot{x}^{\mu} - e g^{\mu\nu} A_{\nu}\right) \left(\dot{x}^{\nu} - e g^{\mu\nu} A_{\mu}\right). \tag{27}$$

In the above equation, $\dot{x}^{\mu}$ represents the four-velocity of the photon, and the dot denotes the derivative with respect to the affine parameter λ along the geodesic. To maintain generality, the photon trajectories are still restricted to the equatorial plane of the black hole, i.e., $\theta = \pi/2$ and $\dot{\theta} = 0$. Furthermore, the Lagrangian is explicitly independent of time t and the azimuthal angle ψ, thus yielding two conserved quantities, energy and angular momentum:

$$E = \frac{\partial \mathcal{L}}{\partial \dot{t}} = f(r)\dot{t} + eA_t, \quad L = \frac{\partial \mathcal{L}}{\partial \dot{\psi}} = r^2 \dot{\varphi}. \tag{28}$$

In the context of a charged Phantom AdS black hole, the Klein–Gordon equation is simplified to the following Hamilton–Jacobi equation [21, 28]:

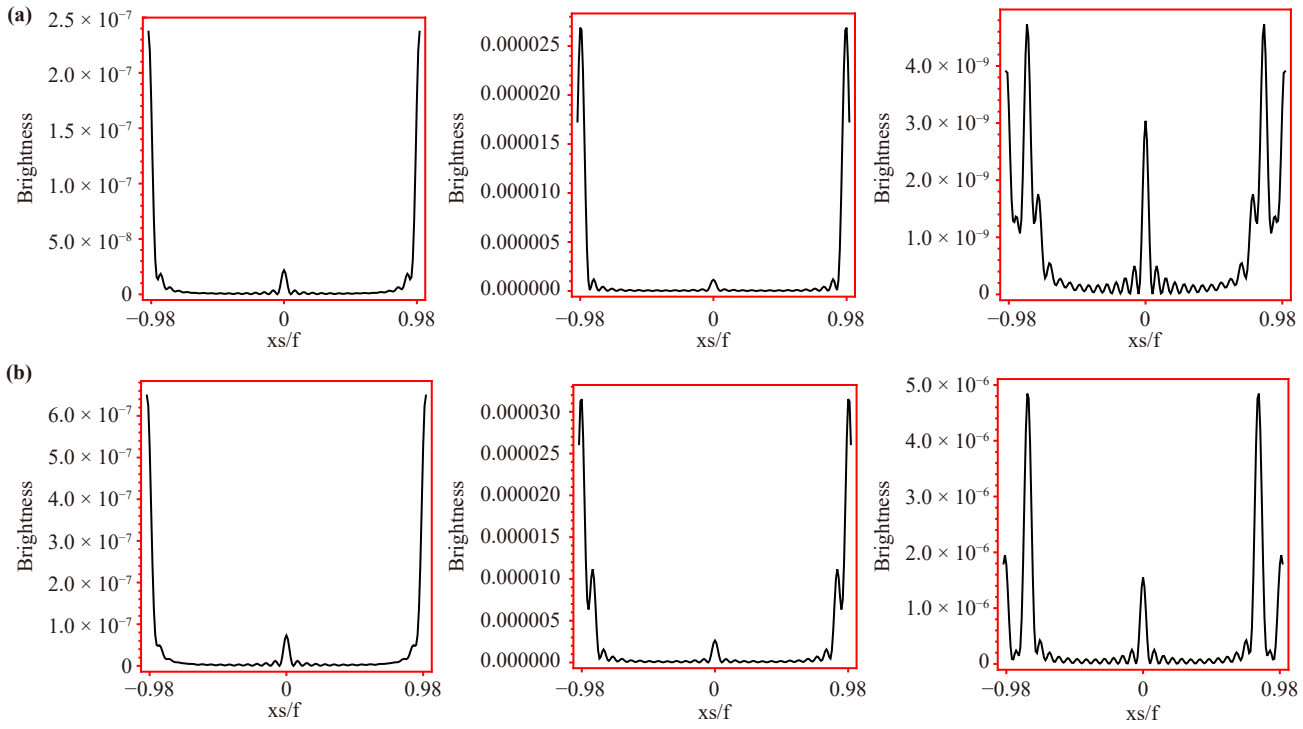

Fig. 10 **(a)** Changes in brightness of the lensed response on the screen for different temperatures T with $\eta = 1$, $\omega = 80$, and $r_h = 0.8$. **(b)** Changes in brightness of the lensed response on the screen for different temperatures T with $\eta = -1$, $\omega = 80$, and $r_h = 0.8$. The values of temperature T from the left panel to the right panel are $T = 0.514767,\ 0.211378,\ 0.119366$, respectively.

$$\frac{1}{2}m^2 = -\frac{1}{2}g^{\mu\nu}\left(\frac{\partial S}{\partial x^\mu} - eA_\mu\right)\left(\frac{\partial S}{\partial x^\nu} - eA_\nu\right), \tag{29}$$

where S represents the action. The Hamilton–Jacobi equation is separable, and its solutions take the form

$$S = -Et + L\psi + \int \frac{\sqrt{\mathbb{R}(r)}}{f(r)}\mathrm{d}r. \tag{30}$$

Here t is the timelike coordinate and ψ is the parameterization of the orbits of the spacelike Killing field. And $\mathbb{R}(r)$ is defined as

$$\mathbb{R}(r) = (E - eA_t)^2 - f(r)(\frac{L^2}{r^2} - 2). \tag{31}$$

Considering the partial derivatives of S with respect to t, ψ, and r, the geodesic trajectories can be further obtained as

$$E = -\frac{\partial S}{\partial t}, L = \frac{\partial S}{\partial \psi}, \frac{\sqrt{\mathbb{R}(r)}}{f(r)} = \frac{\partial S}{\partial r}. \tag{32}$$

It should be noted that for the light rays on the boundary with $n^i = (\frac{\partial}{\partial r^i})$ as the normal vector, the incident angle θ_{in} is given by [20]

$$\cos\theta_{in} = \frac{g_{ij}\upsilon^i\vartheta^j}{|\upsilon||\vartheta|}|_{r=\infty} = \sqrt{\frac{\dot{r}^2/f(r)}{\dot{r}^2/f(r) + L^2/r^2}}|_\infty. \tag{33}$$

Here ϑ represents the 4-velocity of a geodesic, g_{ij} is the induced metric when t is constant, and $|\vartheta|$ and $|\upsilon|$ are the norms of ϑ^i and υ^j with respect to g_{ij}. Therefore, the equivalent relation of Eq. (33) is

$$\sin\theta_{in}^2 = 1 - \cos\theta_{in}^2 = \frac{L^2}{E^2}. \tag{34}$$

The incident angle θ_{in} of the photon orbit at the boundary is

$$\sin\theta_{in} = \frac{L}{E}. \tag{35}$$

At the circular photon orbit of the photon sphere, the above formula remains valid, as shown in Fig. 13. We denote the angular momentum of photons in a critical state as L_p, which can be determined by the condition of the circular photon orbit, that is

$$\mathbb{R}(r) = 0, \frac{\mathrm{d}\mathbb{R}}{\mathrm{d}r} = 0. \tag{36}$$

Furthermore, we can calculate the angle of the Einstein ring, which is the so-called angular distance, as shown in Fig. 14. This angle is displayed on the screen, and its geometric relationship can be expressed as

$$\sin\theta_R = \frac{r_R}{f}. \tag{37}$$

When the angular momentum is sufficiently large,

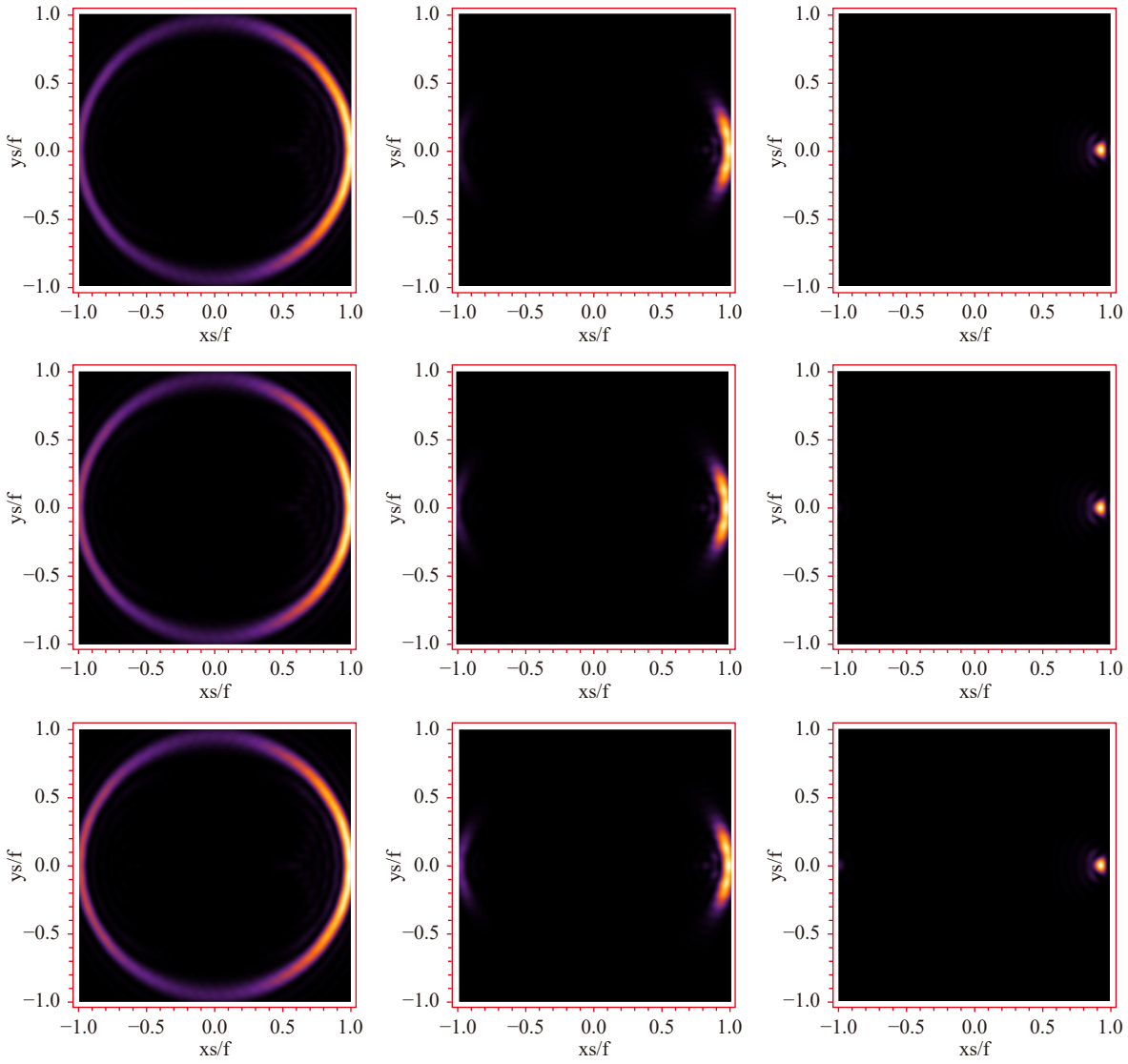

Fig. 11 When the parameter $\eta = 1$, event horizon radius $r_h = 0.8$, and source frequency $\omega = 80$, the lens response image is observed on the screen at different viewing angles. Among them, the observed inclination angles of the first, second, and third columns are $\theta_O = \pi/6$, $\pi/3$, $\pi/2$, and the charge values of the first, second, and third rows are $q = 0.1$, 0.25, 0.5, respectively.

$\sin\theta_{in} = \sin\theta_R$, we have [19, 20]

$$\frac{L_p}{E} = \frac{r_R}{f}. \tag{38}$$

To further verify this relationship, we employed numerical methods for analysis. In Fig. 15, we present the numerical results for the radius of the Einstein ring when $\eta = \pm 1$. Specifically, the blue discrete points r_R/f (in units of f) represent the numerical results of the holographic Einstein ring radius as a function of the radial coordinate r, while the orange curve indicates the radial position of the photon ring r_P. By comparing the results in Fig. 15, the black data points closely surround the orange curve, with the maximum numerical difference 4.5%. Therefore, the Einstein ring angle calculated in the holographic context is highly consistent with the photon incidence angle derived from the geometric optics.

6 Conclusion and discussion

Based on the AdS/CFT correspondence, this paper studies the lensing response generated by the propagation of a complex scalar field as a probing wave in a charged Phantom AdS black hole. Figure 4 displays the absolute amplitude of the response function under different wave sources and gravitational parameters. When the parameter $\eta = 1$ and the wave source frequency ω are relatively low, the corresponding peak amplitude of the response

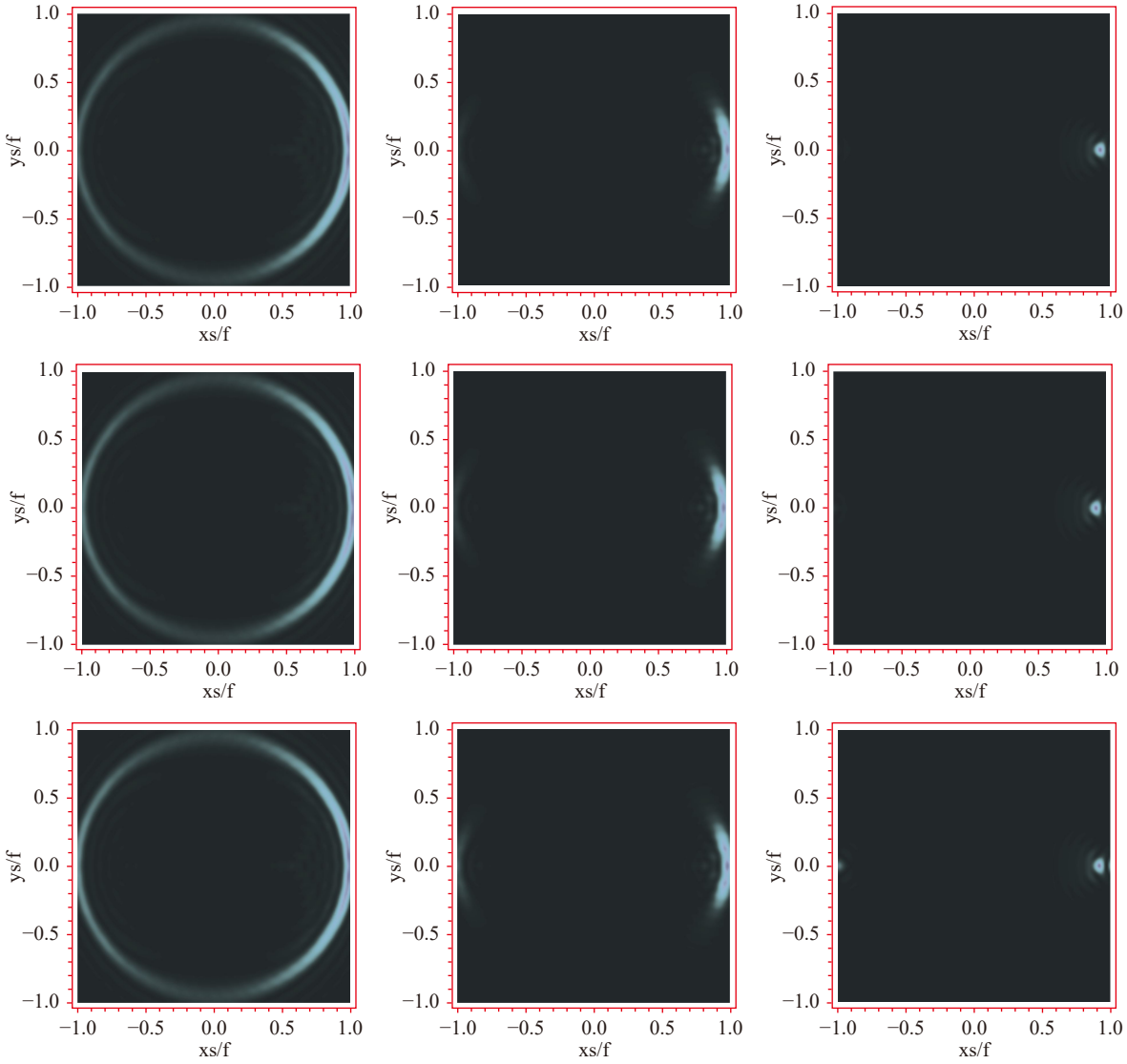

Fig. 12 When the parameter $\eta = -1$, event horizon radius $r_h = 0.8$, and source frequency $\omega = 80$, the lens response image is observed on the screen at different viewing angles. Among them, the observed inclination angles of the first, second, and third columns are $\theta_O = \pi/6$, $\pi/3$, $\pi/2$, and the charge values of the first, second, and third rows are $q = 0.1$, 0.25, 0.5, respectively.

function increases. The case for $\eta = -1$ is similar, except that the peak amplitude of the corresponding response function is greater than that for $\eta = 1$ when other parameters are the same. Additionally, when the wave source frequency ω is low, the period of the scalar wave is larger, and as ω increases, the period of the scalar wave gradually decreases. We then examined the impact of changes in chemical potential on the response function ; when $\eta = 1$ and the chemical potential u approaches a smaller value, the corresponding response function amplitude gradually increases. However, when $\eta = -1$, the amplitude of the response function increases with the increase of the chemical potential u, which is opposite to the case when $\eta = 1$. Furthermore, we investigated the response function under different temperatures T; when $\eta = 1$ and with a relatively high boundary temperature (e.g., $T = 0.514767$), the amplitude reaches its minimum value and sharply increases as the temperature T decreases. For the case of $\eta = -1$, larger amplitude peaks are also observed at lower temperatures T.

To better understand the spacetime of Phantom AdS black holes, we further constructed a virtual optical system in three-dimensional space using a thin convex lens and a hemispherical screen, as shown in Fig. 3. We replicated the response function into the virtual optical system as the incident wave on the lens and established its image on the screen, as shown in Figs. 5(b)–10(b). We observed that when $\theta_O = 0$, regardless of the values of the relevant state parameters, the image of the Phantom AdS black hole always presents a bright annular structure

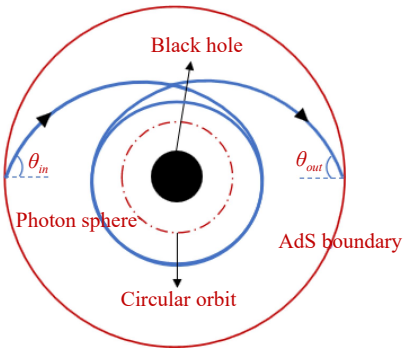

Fig. 13 The ingoing angle and outgoing angle of a ray trajectory in a critical state.

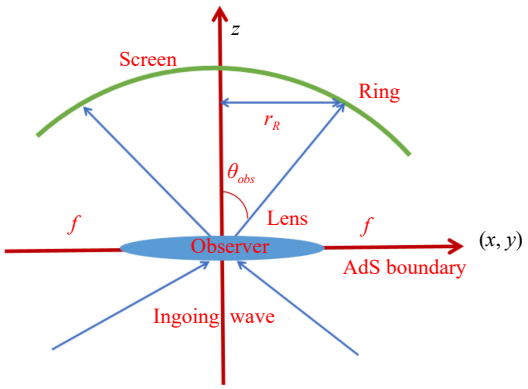

Fig. 14 The correspondence between radius r_R and angle θ_R of the holographic Einstein ring.

on the screen, accompanied by a series of concentric circular stripes, which corresponds to the diffraction of the response function. We further studied the impact of relevant state parameters, such as the wave source frequency ω, chemical potential u, and boundary temperature T, on the Einstein ring image.

When the parameter $\eta = 1$, as the values of ω and T increase, the corresponding ring gradually moves outward, which means the radius of the corresponding ring increases, but an increase in u leads to a decrease in the ring's radius. The brightness curve of the lens response supports this conclusion, as the maximum peak of the brightness curve tends to move away from the center with the increase of ω and T, the decrease of u, and the maximum peak of the curve corresponds exactly to the position of the Einstein ring on the screen. When the parameter $\eta = -1$, the impact of the relevant state parameters on the Einstein ring radius is similar to the case of $\eta = 1$, but the degree of change is greater, and the corresponding brightness curve also verifies this result. On this basis, we illustrated in Figs. 11 and 12 the optical appearance of the Einstein ring when the parameters η, charge q, and observation angle θ_O take different values. When the observation tilt angle is $\theta_O = \pi/6$, the circular structure in the image is broken, and bright arcs appear on both the left and right sides of the screen, with the observed intensity of the right bright arc being significantly greater than that of the left arc. As θ_O increases, such as $\theta_O = \pi/3$, the arc structure on the left side becomes very dark or even disappears. When θ_O approaches $\pi/2$, only an isolated bright spot exists on the right side of the screen, and there is essentially no observable intensity on the left side. Interestingly, when $\eta = -1, \theta_O = \pi/2$, two bright spots appear on the screen, one on each side, but the spot on the left is very dim.

To verify the reliability of these conclusions, we used geometric optics methods to measure the radius of the photon ring and its corresponding incident angle. In Fig. 15, we presented the numerical results of the photon ring position (represented by the orange curve) and the Einstein ring radius (presented by discrete blue points) as a function of the radial coordinate r under different parameter η values. In all the results shown, we observed that the discrete blue points closely surround or exactly fall on the orange curve, which strongly

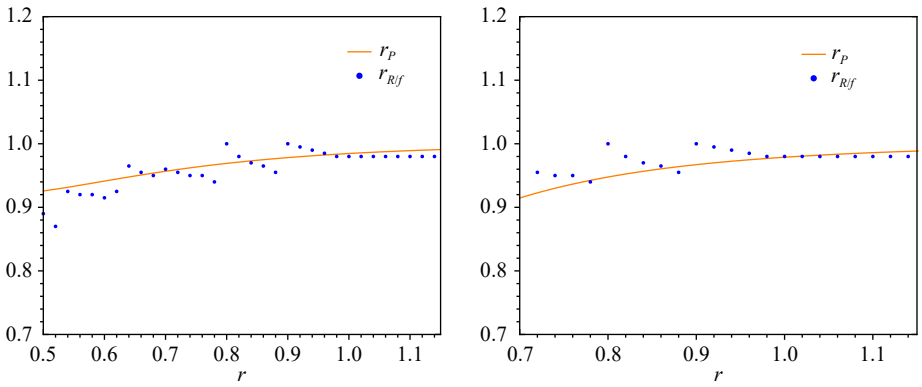

Fig. 15 For different η values ($\eta = 1$ on the left and $\eta = -1$ on the right), the radius of the photon ring (orange curve) and the radius of the Einstein ring in f(discrete blue dot). In addition, the values of other related parameters are fixed as $q = 0.5$ and $\omega = 80$.

supports the consistency of our conclusions with the predictions of geometric optics.

References

1. S. N. Zhang, W. Cui, and W. Chen, Black hole spin in X-ray binaries: Observational consequences, *Astrophys. J.* 482(2), L155 (1997)
2. B. P. Abbott, et al. [LIGO Scientific and Virgo], Observation of gravitational waves from a binary black hole merger, *Phys. Rev. Lett.* 116(6), 061102 (2016)
3. A. Abbott, et al. [LIGO Scientific and Virgo], GW190521: A binary black hole merger with a total mass of $150M_{\odot}$, *Phys. Rev. Lett.* 125(10), 101102 (2020)
4. J. Liu, H. Zhang, A. W. Howard, Z. Bai, Y. Lu, et al., A wide star-black-hole binary system from radial-velocity measurements, *Nature* 575(7784), 618 (2019)
5. K. Akiyama, et al. [Event Horizon Telescope Collaboration], First M87 event horizon telescope results. I. The shadow of the supermassive black hole, *Astrophys. J.* 875(1), L1 (2019)
6. K. Akiyama, et al. [Event Horizon Telescope Collaboration], First M87 event horizon telescope results. II. Array and instrumentation, *Astrophys. J. Lett.* 875(1), L2 (2019)
7. K. Akiyama, et al. [Event Horizon Telescope Collaboration], First M87 event horizon telescope results. III. Data Processing and Calibration, *Astrophys. J.* 875(1), L3 (2019)
8. K. Akiyama, et al. [Event Horizon Telescope Collaboration], First M87 event horizon telescope results. IV. Imaging the central supermassive black hole, *Astrophys. J.* 875(1), L4 (2019)
9. K. Akiyama, et al. [Event Horizon Telescope Collaboration], First M87 event horizon telescope results. V. Physical origin of the asymmetric ring, *Astrophys. J. Lett.* 875(1), L5 (2019)
10. K. Akiyama, et al. [Event Horizon Telescope Collaboration], First M87 event horizon telescope results. VI. The shadow and mass of the central black hole, *Astrophys. J. Lett.* 875(1), L6 (2019)
11. K. Akiyama, et al. [Event Horizon Telescope Collaboration], First Sagittarius A* event horizon telescope results. I. The shadow of the supermassive black hole in the center of the Milky Way, *Astrophys. J.* 930(2), L12 (2022)
12. K. Akiyama, et al. [Event Horizon Telescope Collaboration], First Sagittarius A* event horizon telescope results. II. EHT and multiwavelength observations, data processing, and calibration, *Astrophys. J. Lett.* 930(2), L13 (2022)
13. K. Akiyama, et al. [Event Horizon Telescope Collaboration], First Sagittarius A* event horizon telescope results. III. Imaging of the galactic center supermassive black hole, *Astrophys. J. Lett.* 930(2), L14 (2022)
14. K. Akiyama, et al. [Event Horizon Telescope Collaboration], First Sagittarius A* event horizon telescope results. IV. Variability, morphology, and black hole mass, *Astrophys. J. Lett.* 930(2), L15 (2022)
15. K. Akiyama, et al. [Event Horizon Telescope Collaboration], First Sagittarius A* event horizon telescope results. V. Testing astrophysical models of the galactic center black hole, *Astrophys. J. Lett.* 930(2), L16 (2022)
16. K. Akiyama, et al. [Event Horizon Telescope Collaboration], First Sagittarius A* event horizon telescope results. VI. Testing the black hole metric, *Astrophys. J. Lett.* 930(2), L17 (2022)
17. R. M. Wald, General Relativity, The University of Chicago Press, 1984
18. Y. Nambu, Wave optics and image formation in gravitational lensing, *J. Phys. Conf. Ser.* 410, 012036 (2013)
19. K. Hashimoto, S. Kinoshita, and K. Murata, Einstein rings in holography, *Phys. Rev. Lett.* 123(3), 031602 (2019)
20. K. Hashimoto, S. Kinoshita, and K. Murata, Imaging black holes through the AdS/CFT correspondence, *Phys. Rev. D* 101(6), 066018 (2020)
21. Y. X. Liu, Q. Chen, X. X. Zeng, H. B. Zhang, and W. L. Zhang, Holographic Einstein ring of a charged AdS black hole, *J. High Energy Phys.* 2022(10), 189 (2022)
22. Y. Kaku, K. Murata, and J. Tsujimura, Observing black holes through superconductors, *J. High Energy Phys.* 2021, 138 (2021)
23. X. Y. Hu, M. I. Aslam, R. Saleem, and X. X. Zeng, Dynamics of holographic images of scalar-tensorvector gravity-AdS black holes, *Chin. Phys. C* 48(9), 095108 (2024)
24. X. Y. Hu, X. X. Zeng, L. F. Li, and P. Xu, Holographic Einstein rings of non-commutative black holes, *Eur. Phys. J. C* 84(2), 199 (2024)
25. X. X. Zeng, K. J. He, J. Pu, G. P. Li, and Q. Q. Jiang, Holographic Einstein rings of a Gauss–Bonnet AdS black hole, *Eur. Phys. J. C* 83(10), 897 (2023)
26. G. P. Li, K. J. He, X. Y. Hu, and Q. Q. Jiang, Holographic images of an AdS black hole within the framework of $f(R)$ gravity theory, *Front. Phys. (Beijing)* 19(5), 54202 (2024)
27. K. J. He, Y. W. Han, and G. P. Li, Holographic image features of Hayward–AdS black hole surrounded by quintessence dark energy, *Phys. Dark Univ* 44, 101468 (2024)
28. X. Y. Hu, X. X. Zeng, L. F. Li, and P. Xu, Holographic study on Einstein ring for a charged black hole in conformal gravity, *Results Phys.* 61, 107707 (2024)
29. G. P. Li, K. J. He, X. Y. Hu, and Q. Q. Jiang, Holographic images of an ads black hole within the framework of $f(r)$ gravity theory, *Front. Phys. (Beijing)* 19(5), 54202 (2024)
30. L. Shao, Imaging supermassive black hole shadows with a global very long baseline interferometry array, *Front. Phys. (Beijing)* 17(4), 4 (2022)
31. Z. M. Xu, Analytic phase structures and thermodynamic curvature for the charged AdS black hole in alternative phase space, *Front. Phys. (Beijing)* 16(2), 7 (2021)
32. J. Dunkley, E. Komatsu, M. R. Nolta, D. N. Spergel, D. Larson, et al., Five-year Wilkinson Microwave Anisotropy Probe (WMAP) Observations: Likelihoods and Parameters from the WMAP data, *Astrophys. J. Suppl. Ser.* 180(2), 306 (2009)
33. S. Hannestad, Dark energy and dark matter from cosmological observations, *Int. J. Mod. Phys. A*

21(08–09), 1938 (2006)
34. K. Komatsu, K. M. Smith, J. Dunkley, C. L. Bennett, B. Gold, et al., Seven-year Wilkinson Microwave Anisotropy Probe (WMAP) observations: Cosmological interpretation, *Astrophys. J. Suppl. Ser.* 192(2), 18 (2011)
35. P. Singh, M. Sami, and N. Dadhich, Cosmological dynamics of phantom field, *Phys. Rev. D* 68(2), 023522 (2003)
36. G. W. Gibbons and D. A. Rasheed, Dyson pairs and zero mass black holes, *Nucl. Phys. B* 476(3), 515 (1996)
37. M. Azreg-Ainou, G. Clement, J. C. Fabris, and M. E. Rodrigues, Phantom black holes and sigma models, *Phys. Rev. D* 83(12), 124001 (2011)
38. M. Azreg-Ainou, Light paths of normal and phantom Einstein–Maxwell-dilaton black holes, *Phys. Rev. D* 87(2), 024012 (2013)
39. G. N. Gyulchev and I. Z. Stefanov, Gravitational lensing by phantom black holes, *Phys. Rev. D* 87(6), 063005 (2013)
40. D. F. Jardim, M. E. Rodrigues, and M. J. S. Houndjo, Thermodynamics of phantom Reissner–Nordstrom–AdS black hole, *Eur. Phys. J. Plus* 127(10), 123 (2012)
41. J. X. Mo and S. Q. Lan, Phase transition and heat engine efficiency of phantom AdS black holes, *Eur. Phys. J. C* 78(8), 666 (2018)
42. X. X. Zeng, X. Y. Hu, and L. F. Li, Effect of phantom dark energy on holographic thermalization, *Chin. Phys. Lett.* 34(1), 010401 (2017)
43. M. U. Shahzad, S. Khalid, and A. Övgün, Motion of spinning particles around dynamic phantom AdS black holes, *Eur. Phys. J. C* 83(11), 1031 (2023)